



Picosecond laser beam nanostructuring of GDC thin films: exchange surface enhancement by LIPSS

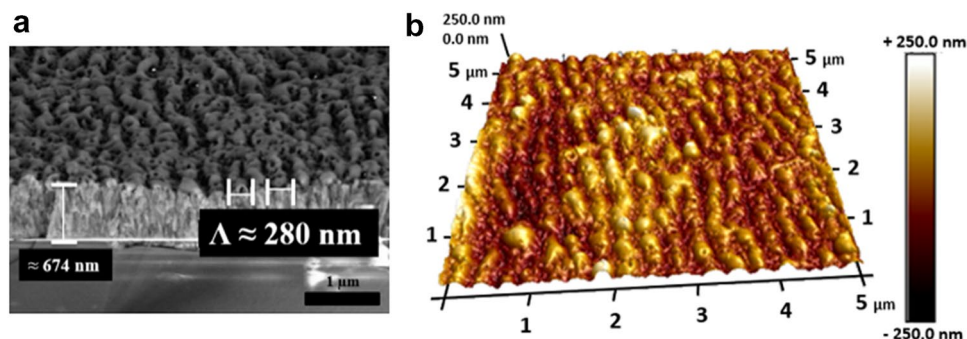
Wael Karim¹ · Agnès Petit¹ · Hervé Rabat¹ · Malek Tabbal² · Anne-Lise Thomann¹ · Nadjib Semmar¹

Received: 7 June 2022 / Accepted: 6 July 2022 / Published online: 2 August 2022
© The Author(s), under exclusive licence to Springer-Verlag GmbH, DE part of Springer Nature 2022

Abstract

In ceramic electrochemical cells, gadolinium-doped ceria (GDC) thin film is deposited between the electrolyte (yttria-stabilized zirconia, YSZ) and the upper electrode to improve the aging resistance. Increasing the interface surface area is expected to be beneficial to the cell performance. This work investigates the formation of LIPSS (Laser induced periodic surface structures) on the surface of a 600 nm GDC thin films grown by magnetron sputtering on screen-printed YSZ. A picosecond Nd:YAG laser operating at its third harmonic ($\lambda = 355$ nm, 40 ps, 10 Hz) was used to structure the surface of the GDC/YSZ layer after deposition, thanks to static and scanning irradiation modes. The different structures formed on the film surface following laser irradiation, mainly quasi-periodic LIPSS, were investigated by scanning electron microscopy (SEM) and atomic force microscopy (AFM). Parallel and perpendicular LIPSS were simultaneously formed with periods varying from 220 to 300 nm, as a function of the beam fluence ranging from 30 to 160 mJ/cm², and within a spot size of ~ 500 μ m in the static mode. The coexistence of the two orientations disappeared at a higher number of shots ($N > 20$), where only parallel structures were formed. Increasing the number of shots up to $N > 50$ led to a progressive ablation of the film followed by the start of a process of YSZ substrate nano-structuring. The formation of parallel LIPSS is mainly attributed to the thermochemical process that occurs on the GDC/YSZ film in the center of the irradiated zone corresponding to the highest local fluence. The same LIPSS orientations were also found in the scanning mode by varying the laser fluence and the scanning stage parameters. For the latter mode, the effect of laser irradiation on the elemental composition of the films was investigated by energy dispersive X-ray spectroscopy (EDX) and Rutherford back-scattering (RBS) to check the film chemical stability under the process of soft ablation by accumulation effect. Finally, the surface area enhancement by LIPSS formation was estimated thanks to atomic force microscopy (AFM) and using a geometrical enhancement coefficient that returned ‘theoretical’ maximum values of 57% and 78% for 1D (regular LIPSS) and 2D periodic structures, respectively, and 41% for the experimental case.

Graphical abstract



Keywords Picosecond laser beam · Oxide thin film · GDC magnetron sputtered film · Multi-pulse irradiation · LIPSS

Extended author information available on the last page of the article

1 Introduction

The interaction between ultrashort laser beam pulses and solid-state materials can result in the formation of surface micro/nanostructures that are commonly referred to as Laser Induced Periodic Surface Structures (LIPSS). The size, shape and distribution of these structures show a complex dependence on the experimental conditions (such as laser energy, wavelength, repetition rate, scanning speed) as well as the type of material irradiated (metals, semiconductor, dielectric, ceramic or polymer) [1–7]. An understanding of LIPSS formation and a good control of their characteristics is crucial, since their presence significantly modifies the surface properties of the material, which can thus be “tuned” for a specific application. LIPSS formation has indeed been shown to improve the mechanical and wetting properties of surfaces in addition to several other applications in a wide array of technological fields [8–13]. Building on the potential of laser texturing of the surface of bulk material, LIPSS formation on thin films has recently generated great interest both from the fundamental and technological aspects [14–17]. Compared to the case of bulk materials, the physico-chemical processes occurring during the laser irradiation of a thin film are markedly altered, typically with the observation of, for example, a lowering of the material’s ablation threshold, the occurrence of cavitation as well as thermomechanical fragmentation [18–21]. From a technological viewpoint, LIPSS formation on thin films could provide an attractive one-step approach to material micro/nano-structuring for functional coatings and advanced devices.

This work deals specifically with the investigation of LIPSS formation on the surface of gadolinium-doped ceria (GDC) thin films grown by magnetron sputtering on screen-printed yttria-stabilized zirconia (YSZ). GDC and YSZ are complex oxides that are employed in solid ceramic cell technology [22–24] due to their high ionic conductivity. A thin layer of GDC sandwiched between the electrolyte and the upper electrode ($\text{La}_{1-x}\text{Sr}_x\text{Co}_{1-y}\text{Fe}_y\text{O}_{3-\delta}$) can act as a diffusion barrier and has been found to improve the lifetime of cells dedicated to the production of hydrogen by high temperature electrolysis. With the aim of improving the efficiency of the cell, one interesting approach would be to increase the surface area, where the electrochemical reactions take place, namely, the actual area of the interface between the electrolyte (YSZ) and the upper electrode. In the present study, a picosecond Nd:YAG laser operating at the third harmonic ($\lambda = 355$ nm) was used to structure the surface of the GDC layer after deposition, both in static and scanning modes. The different structures formed on the film surface following laser irradiation were investigated by scanning

electron microscopy (SEM) and atomic force microscopy (AFM) with tapping mode. A mapping of the different surface morphologies as a function of irradiation conditions was thus achieved for the static mode. The effect of laser irradiation on the elemental composition of the films was also investigated by energy dispersive X-ray spectroscopy (EDX) and Rutherford back-scattering (RBS). Lastly, surface area enhancement by LIPSS formation is discussed using a simple model based on the morphological arrangement of the induced nanostructures.

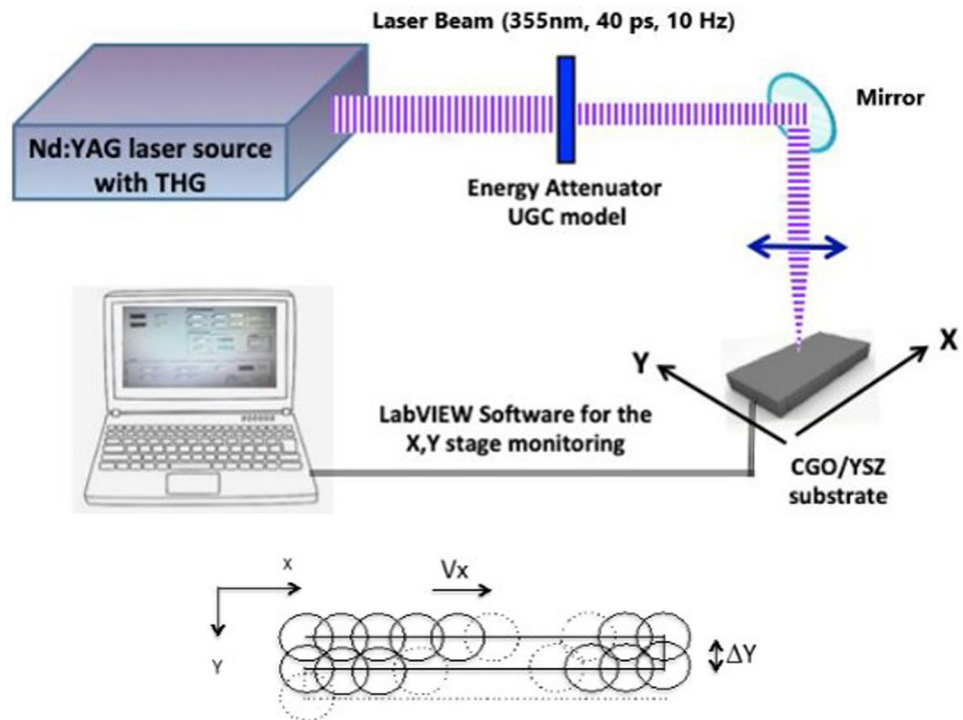
2 Experimental

Gadolinium-doped ceria (GDC) thin films, with thicknesses of around 600 nm were deposited by direct current magnetron sputtering of 4-inch diameter metallic $\text{Ce}_{1-x}\text{Gd}_x$ targets ($x = 0.2$) on screen-printed Yttrium-Stabilized Zirconium (YSZ) substrates (having thicknesses ≥ 1 μm) provided by the CEA Le Ripault. All deposition runs were performed at a pressure of 1 Pa with 20 sccm of Ar as a sputtering gas and 2 sccm of O_2 as a reactive gas. The substrates were not heated during growth. The as-deposited films were subsequently annealed in air at 500 °C, a process that resulted in highly crystalline and stoichiometric layers ($\text{Ce}_{1-x}\text{Gd}_x\text{O}_2$). More details about growth conditions and film properties were presented elsewhere by Mickan et al. [25].

The laser irradiation experiments were achieved using a picosecond Nd:YAG laser operating at its third harmonic ($\lambda = 355$ nm) with a pulse duration of 40 ps and 10 Hz repetition rate. The corresponding irradiation process is shown in Fig. 1. The energy/pulse is modulated using a set of optical filters (UGC from Thorlabs), and the Gaussian beam of the laser is then focused on the surface of the sample using a quartz lens with a focal distance of 75 mm. For the present study, the laser fluence of the incident beam (F) was varied from 30 to 125 mJ/cm^2 .

Samples were irradiated in static mode (by accumulation of successive single spots) and in scanning mode (large-area irradiation achieved by S-scanning) in air under atmospheric conditions. In static mode, the total number of shots (N) irradiating the same area of the sample is accurately controlled via an automated opto-mechanical shutter. Under scanning mode conditions, the sample is mounted on a motorized X, Y computer-controlled scanning stage. To irradiate the whole surface of the films, an S-shaped scanning pattern is achieved via a LabVIEW interface. Thanks to an automated scanner system (Scanner Newport–Conex CC with accessible speed ranging from 0.01 to 5 mm/s in the X, Y directions, with a translation path $\Delta Y = 100$ μm), the sample is moved along the x -axis at a speed V_x and displaced by a distance ΔY (perpendicular to the x -axis) at the end of the motion.

Fig. 1 Schematic of experimental setup process for GDC laser texturing, and (below) the corresponding S-scanning mode



The values of V_x used in the work were varied from 50 $\mu\text{m/s}$ up to 5 mm/s.

The surface morphology of the thin films before and after laser irradiation was observed using a Carl Zeiss SMT SUPRA 40 Field Emission Gun SEM, and their chemical composition determined using EDX. LIPSS amplitude and periodicity were determined through surface imaging using a Bruker AFM. Finally, RBS analysis was performed using α particles of 2 MeV extracted from a Pelletron accelerator in the CEMHTI laboratory (CNRS-Orléans, France).

3 Results

3.1 Irradiation under static mode

Figure 2 shows a typical SEM image of the surface of a GDC film irradiated under static mode with 10 laser pulses at a fluence of 125 mJ/cm^2 and a large spot size close to 500 μm . Careful observation enables several different regions on the image to be delimited, corresponding to the insets within the figure. First, the non-irradiated surface of the GDC films exhibits the grain boundaries of the polycrystalline YSZ layer (micron-sized grains) decorated by the GDC film [25]. The laser impact region, reasonably approximated to be circular with a diameter $W_0 \approx 500 \mu\text{m}$, can be distinguished within which, two nearly circular concentric regions were imaged by SEM at higher resolution (see insets). The two different regions correspond to the formation of unexpected

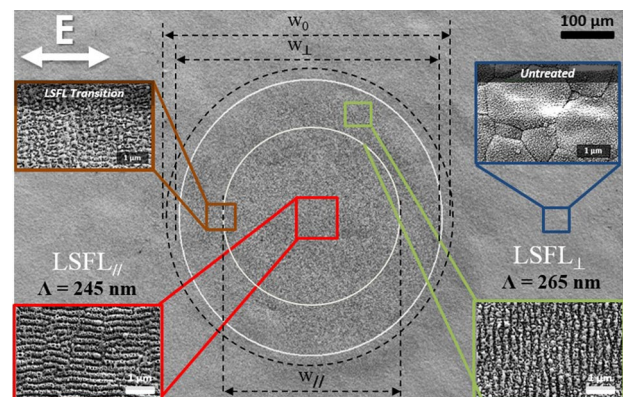


Fig. 2 SEM image of the irradiated CDG film, for $F=125 \text{ mJ/cm}^2$ and $N=10$ pulses. The insets show the non-irradiated (untreated) surface as well as two different LIPSS patterns (LSFL_{\parallel} and LSFL_{\perp}) and the transition zone. W_0 is the beam spot size; W_{\perp} and W_{\parallel} are the estimated diameters of LSFL_{\perp} and LSFL_{\parallel} regions, respectively

periodic patterns having different orientations with respect to the beam polarization. Quasi-regular LIPSS with orientation perpendicular to the laser beam (see bottom inset of the figure) are visible on the border of the irradiated zone. These LIPSS are formed at lower energy density (keeping in mind the beam Gaussian distribution) and are found to have a spatial period $\Lambda \sim 265 \pm 10 \text{ nm}$, lower than the laser wavelength ($\lambda = 355 \text{ nm}$), and denoted as LSFL_{\perp} . In the center of the laser spot, which corresponds to the highest local fluence, unexpected LIPSS oriented parallel to the polarization of

the laser beam with a spatial period of about 245 ± 10 nm are also observed and denoted as $\Lambda_{\text{LSFL}_{//}}$, as indicated in the bottom inset of Fig. 2. The formation of two LIPSS patterns with different spatial periods and different directions was already observed in the case of HSFL and LSFL formation within the same spot zone [26] [27], on several metal and dielectric materials as well as on polymer thin films [28–30] but was rarely evidenced on a complex oxide substrate with such close spatial periods. Using a similar picosecond laser at the fourth harmonic (266 nm), Huynh et al. [16] found LSFL with a period of 260 nm on the surface of a Cu thin film. After increasing the number of shots to very high values, HSFL and LIPSS dots were formed. Considering another metallic film but under scanning mode, Dostovalov et al. [31] found on the Cr surface, irradiated with a femtosecond laser ($\tau = 232$ fs; $\lambda = 1026$ nm; $f = 200$ kHz), LSFL-like structures ($\Lambda_{\text{LSFL}} = 696, 704, 816,$ and 858 nm) for a scanning speed $V = 1, 10, 50$ and 100 $\mu\text{m/s}$, respectively. In both studies, the LSFL obtained were in the range $(0.6\text{--}0.9)\lambda$, parallel to the laser beam polarization, which is very similar to our unexpected case of $\Lambda_{\text{LSFL}_{//}}$ structures. On the contrary, Talbi et al. [17] managed to texture a thin layer of dielectric (titanium oxide $\text{TiO}_{1.2}$) and obtained LSFL structures perpendicular to the beam polarization with a period of 800 nm, using a femtosecond laser with a wavelength of 1030 nm and a pulse duration of 500 fs. As reported earlier in several theories debating on the LIPSS mechanism [12, 32, 33], the formation of LIPSS parallel or perpendicular to the laser beam polarization is mainly related to the nature of the material surface (electronic, optical, thermal properties, etc.) and the laser beam features (polarization, intensity, repetition rate, etc.). Dostovalov et al. [34] studied the mechanism of LIPSS formation in Cr thin film material subject to oxidation. The oxidation level (depending on the film thickness) during the irradiation was found to induce a significant change in the optical properties as a consequence of the physico-chemical nature of the oxide film, and thus in the LIPSS orientation, parallel or perpendicular to the beam polarization. The particular ‘thermochemical’ conditions leading to oxidation during the irradiation of thin metal films were also investigated by Oktem et al. [35] on Ti thin films. The authors proposed a new paradigm through the ‘positive feedback’ approach for highly regular LIPSS formation. In such cases, the nanostructures formed were identified as thermochemical LIPSS (TLIPSS). To support this assumption (TLIPSS formation) for the $\Lambda_{\text{LSFL}_{//}}$ formed on GDC/YSZ in the center of the irradiated zone further chemical investigations are needed, for example, using XPS analysis (not shown in the present work) for an accurate estimation of the oxygen contribution. Moreover, it has been found in the literature that above 700 $^{\circ}\text{C}$, annealed GDC can lose part of its oxygen content. This leads to an increase in the non-stoichiometric coefficient δ ($\text{Ce}_{0.8}\text{Gd}_{0.2}\text{O}_{2-\delta}$), which can induce a lattice

expansion, commonly referred to as “chemical expansion”. This may originate from the growth of the cation radii during the reduction reactions taking place inside the CGO layers [36, 37]. Thus, the Ce^{4+} ions incorporated in CGO transform into Ce^{3+} ions, which can locally generate a mixed ionic electronic conductivity (MIEC) [38]. As previously mentioned, due to the Gaussian beam distribution, the local fluence is highest at the center of the laser spot, so that the temperature can locally exceed the value (considering also the reaction time over this temperature threshold) at which GDC acquires MIEC properties. This could induce a *transient* ‘metallic’ behavior followed by intense back-oxidation that probably induces the formation of $\Lambda_{\text{LSFL}_{//}}$.

Further inspection of the LIPSS formation at different laser fluences led to finding a dependence of the LIPSS spatial period on laser fluence as shown in Fig. 3 for both types of LIPSS, $\Lambda_{\text{LSFL}_{//}}$ and $\Lambda_{\text{LSFL}_{\perp}}$. The figure shows that the spatial periods for each type move closer to each other as the laser fluence is increased from 60 to 125 mJ/cm^2 , increasing (decreasing) from 220 (300) to 245 (265) nm, respectively. The values of the spatial periods thus range from 0.6λ to 0.85λ , and these are known to depend on the refractive index n of the irradiated material. This also tends to confirm the correlation between the oxidation stage, the chemical expansion and thus the changes in optical properties. Thanks to the results reported in Dostovalov et al. [34], the diminution of the $\Lambda_{\text{LSFL}_{\perp}}$ period versus fluence can be related to the ‘soft’ ablation process and the reduction in film thickness, while the slight increase in the $\Lambda_{\text{LSFL}_{//}}$ period is attributed to chemical expansion followed by more intense re-oxidation.

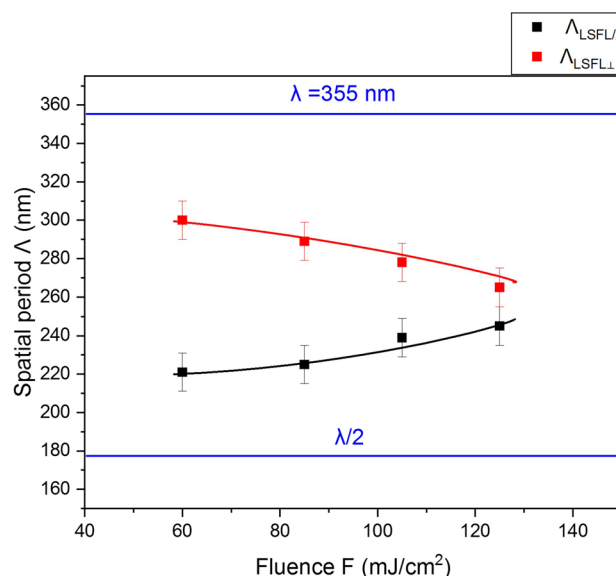


Fig. 3 Spatial period of parallel ($\Lambda_{\text{LSFL}_{//}}$) and perpendicular ($\Lambda_{\text{LSFL}_{\perp}}$) LIPSS as a function of the laser fluence F under static irradiation with 10 pulses

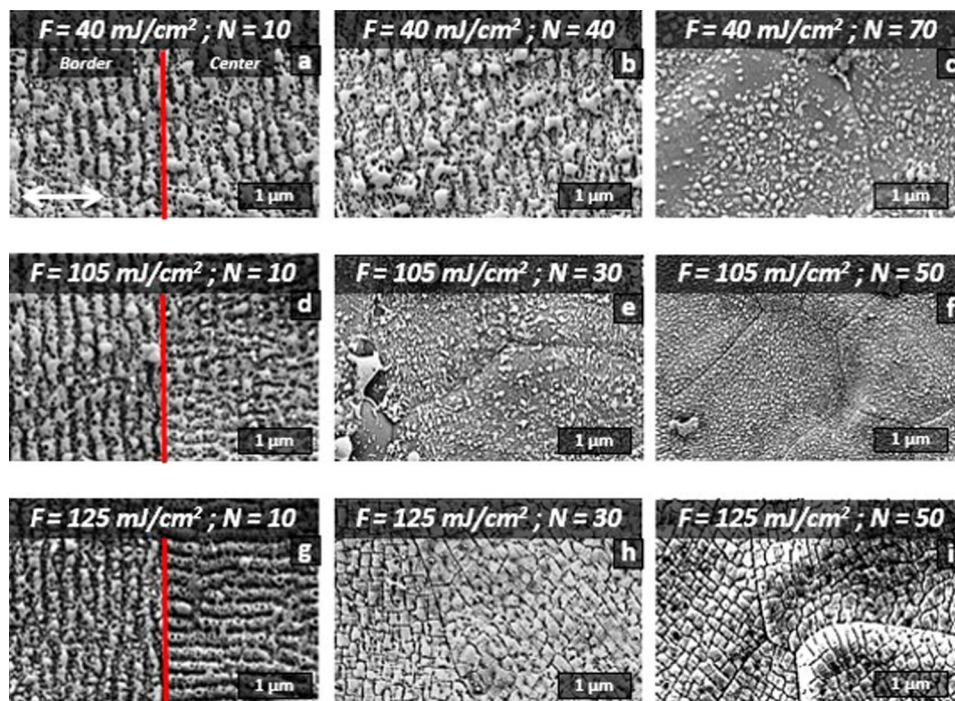
Note that in such a complex situation, intermediate 2D-like structures are localized in the transition zone between the center and rim of the irradiated zone as previously shown in Fig. 2.

To investigate the (F, N) domain of LIPSS formation and their singular orientation, the fluence and the number of shots were regularly increased up to complete ablation of the GDC film. Figure 4 shows SEM images of the surface of the GDC/YSZ samples irradiated at laser fluences between 40 and 125 mJ/cm², and numbers of shots ranging from 10 to 70. Different surface morphologies are observed depending on the laser fluence and number of laser pulses. At the lowest fluence, namely, 40 mJ/cm², LSFL_⊥ are observed at *N*=10 and *N*=40, Fig. 4a, b, respectively. In the latter case, however, the LIPSS do not appear to be regularly formed. Increasing the number of pulses to 70 leads to the loss of the LIPSS patterns by ablation and re-deposition of the GDC films (Fig. 4c). On increasing the laser fluence to 105 and 125 mJ/cm², both parallel and perpendicular LIPSS are still formed, as shown in Fig. 4d, g, where the reported SEM images were taken at different places of the irradiated area (separated by the red line in the figure). As shown before, the LSFL_⊥ were found near the borders of the laser spot, and the LSFL_∥ appear in the center. Static irradiation with 30 pulses at 105 mJ/cm² leads to the loss of the LIPSS pattern (Fig. 4e) and this becomes more pronounced after 50 pulses (Fig. 4f), where the crystalline grain boundaries of the underlying YSZ become exposed. It is noteworthy that the loss of the LIPSS pattern takes place at a smaller number of pulses with increasing laser fluence, i.e., at 30 laser

pulses at 105 mJ/cm² instead of 70 for a laser fluence of 40 mJ/cm². At even higher fluence, 125 mJ/cm², and after 30 and 50 laser pulses, the GDC film appears to be completely ablated and is accompanied by patterning of the YSZ into square shapes.

The chemical composition of the surfaces after laser irradiation was investigated using EDX analysis. To that end, the representative signals for films irradiated at different laser fluences and number of laser pulses are reported in Fig. 5, along with that of the untreated film. The insets included in the figure correspond to the SEM images shown in Fig. 4. On the EDX spectra of the untreated sample (Fig. 5a) and that of a film irradiated with 10 pulses at 40 mJ/cm² (Fig. 5b) exhibiting LIPSS, similar Ce and Gd signals are detected, whereas no signal emanating from the underlying YSZ substrate is evidenced. This confirms that the LIPSS patterns formed retain, within the accuracy limit of EDX, the same chemical composition as the starting material. With the loss of LIPSS formation for *N*=70 at the same laser fluence (Fig. 5c), the EDX signals from the Ce and Gd become very low and in addition a broad peak corresponding to Y and Zr (the overlapping signals from these two elements is due to their close atomic masses, 89 and 91 u) is detected. This confirms the onset of ablation suggested from the SEM image for these irradiation conditions (Fig. 4c). The same trends are visible in Fig. 5d for a laser fluence of 150 mJ/cm² and a number of pulses of 40. This confirms that the square-shaped pattern seen in the inset of Fig. 5d can be attributed to laser surface structuring of the YSZ substrate (though some traces of the GDC film may remain). These

Fig. 4 SEM images of the GDC/YSZ films irradiated in static mode for different fluence values and number of pulses (a–i). Horizontally, the laser fluence is fixed and the number of laser pulses is increased from 10 to 40 then 50 or 70. Vertically, the laser fluence is increased from 40 to 105 then to 125 mJ/cm². For d and g, the upper (lower) images were taken at the border (center) of the laser spot



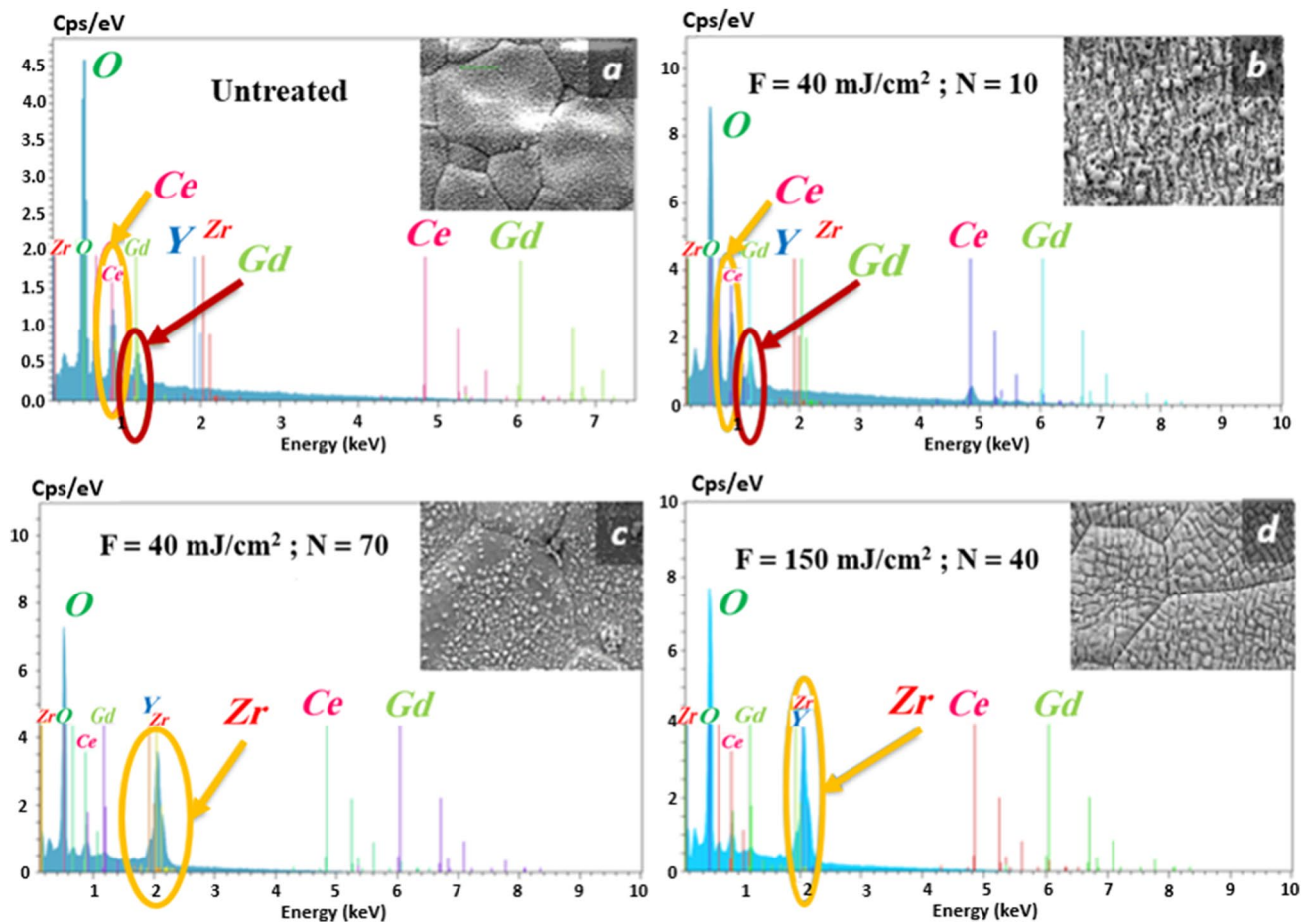


Fig. 5 EDX signals of the **a** untreated GDC film and films irradiated under different static laser conditions (**b–d**). SEM images of the corresponding film surfaces are also shown in the inset of each EDX spectrum

patterns are quite similar to those obtained at 125 mJ/cm^2 for $N=30$ and 50 , Fig. 4h and i, and evidence the almost complete ablation of the GDC film.

Based on the parametric study presented above, a mapping of the laser induced surface modification of the GDC films grown on YSZ is suggested in Fig. 6, as laser fluence and number of laser pulses are varied from 30 to 150 mJ/cm^2 and 1 – 70 , respectively. The SEM and EDX observations allow us to delimit five distinguishable domains whose formation is dependent on the local energy dose.

In summary: LIPSS formation is not possible for $F < 40 \text{ mJ/cm}^2$ (presented in gray). At higher fluence values (85 to 125 mJ/cm^2), $\text{LSFL}_{//}$ and LSFL_{\perp} (in red) were generated but with $N < 20$.

Each phenomenon exists in a given area of the plot, i.e., over a given range of fluence and number of laser pulses. For instance, ablation occurs at a higher laser pulse number when the fluence is decreased. This is an indication that the ablation threshold is related to a parameter proportional to $F \times N$ (total deposited energy dose), which is the sign of an

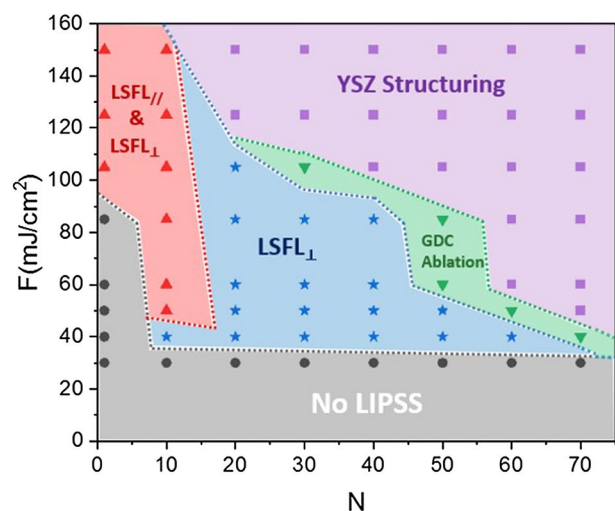
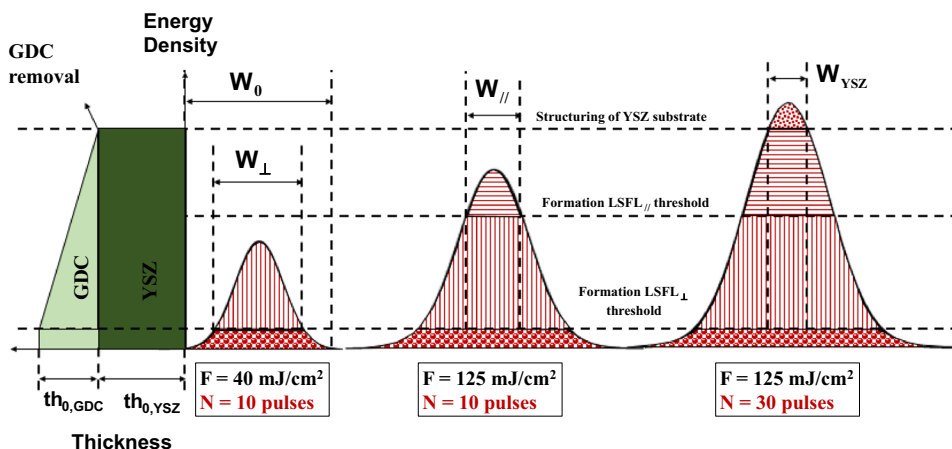


Fig. 6 Mapping of the laser induced surface modification of GDC on YSZ depending on laser fluence (y-axis) and number of laser pulses (x-axis)

Fig. 7 Schematic view of the dependence of the LSFL formation typology for three regimes applied on the GDC surface. W_{YSZ} is the threshold diameter that corresponds to full GDC ablation/YSZ structuring. The progressive ablation of the GDC/YSZ film is shown on the diagram versus the energy dose



incubation phenomenon. The same behavior is observed for the formation of both kinds of LSFL. In Fig. 7, we present a schematic that depicts the various energy dose thresholds for the formation of perpendicular and parallel LIPSS as well as the threshold for GDC full ablation that also corresponds to the starting point of YSZ structuring.

3.2 Irradiation under scanning mode

To estimate the enhancement of the exchange area on an extended treated surface of GDC film we performed laser irradiation on a wide surface area (minimum $4 \times 4 \text{ mm}^2$) by moving the sample holder in the X, Y directions, as indicated in Fig. 1.

The starting point of our scanning strategy is based on the (F, N) mapping plot (Fig. 6) to reproduce on a large scale the LIPSS with the two main findings of the static mode: $F = 125 \text{ mJ/cm}^2, N < 20$ conditions corresponding to the co-existence of $LSFL_{\parallel}$ and $LSFL_{\perp}$, and $F = 85 \text{ mJ/cm}^2, 20 < N < 30$ conditions to lie in the pure $LSFL_{\perp}$ domain. Results for both operating conditions are plotted in Fig. 8 when the N becomes N_{eff} calculated from a standard formula that links the repetition rate f and the spot size d to the scanner speed V_x and the transverse path ΔY (i.e.,

$N_{\text{eff}} = (d \times f) / V_x \times (d / \Delta Y)$). As shown on the corresponding SEM images, while the first condition reproduces similar regular structures as in the static mode, the second one ($F = 125 \text{ mJ/cm}^2, N_{\text{eff}} = 10$) shows more complex patterns due to the superposition of parallel and perpendicular LSFL induced by the overlap of the successive irradiations. We also conducted the same EDX analyses as for the static mode with similar conclusions for the CGO film. However, some redeposition is observed for the higher fluence ($F = 125 \text{ mJ/cm}^2$), suggesting that a deeper investigation of the limit parameters is required to achieve full ablation of the film.

For this purpose, we investigated laser irradiation of the GDC films for $F = 40, 85, 125$ and 150 mJ/cm^2 under two (low) scanning speeds 0.2 and 0.4 mm/s ($N_{\text{eff}} = 125, 65.5$, respectively). SEM images of these laser irradiated surfaces are shown in Fig. 9. For $F = 40 \text{ mJ/cm}^2$, no LIPSS are detected for a scanning speed of 0.4 mm/s (Fig. 9a1) but some regular rippling indicating the onset of LIPSS formation is observed at 0.2 mm/s , (Fig. 9a2). Increasing the value of laser fluence to 85 mJ/cm^2 , LIPSS are formed even at the higher scanning speed of 0.4 mm/s (Fig. 9b1) and appear somewhat similar to those obtained at 0.2 mm/s (Fig. 9b2). This implies that the energy threshold to obtain LIPSS is reached even at the highest speed. A further increase of

Fig. 8 SEM images showing the comparison of two irradiation conditions in scanning mode related to the static mode by the effective number of pulses N_{eff}

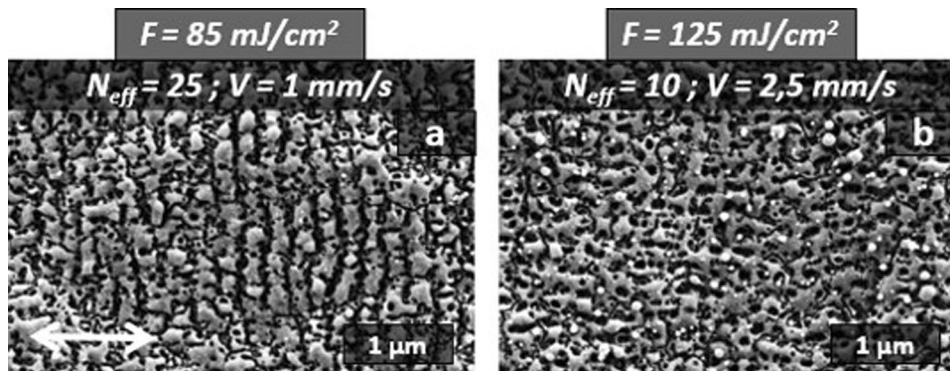
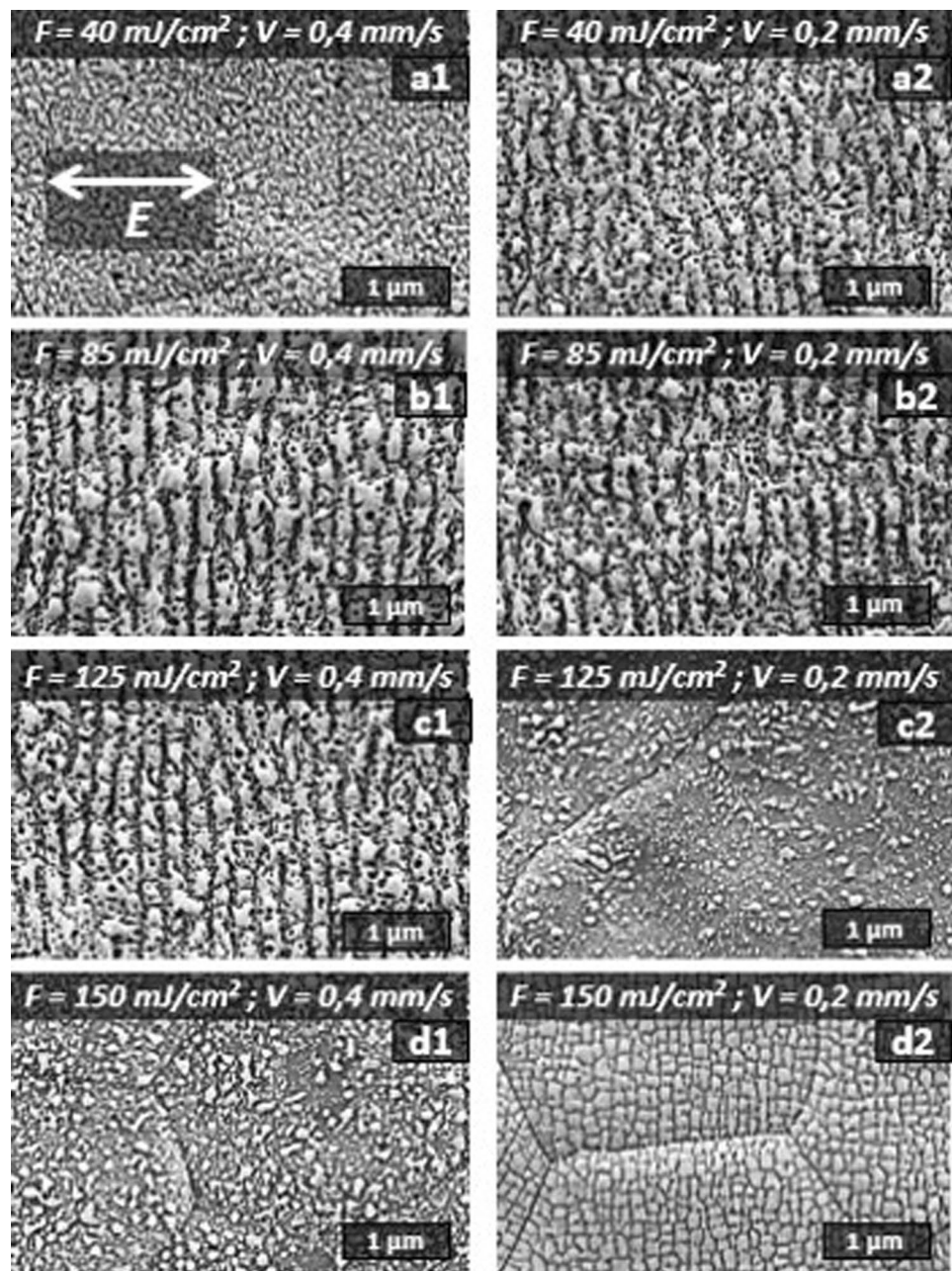


Fig. 9 SEM images showing the evolution of the surface of the GDC/YSZ films irradiated in scanning mode for different laser fluences and scanning speeds (a1–d2). Horizontally, the laser fluence is fixed and the scanning speed is varied from 0.4 to 0.2 mm/s. Vertically, the scanning speed is fixed and the laser fluence is increased from 85 to 150 mJ/cm². Laser polarization is shown as the two-headed white arrow

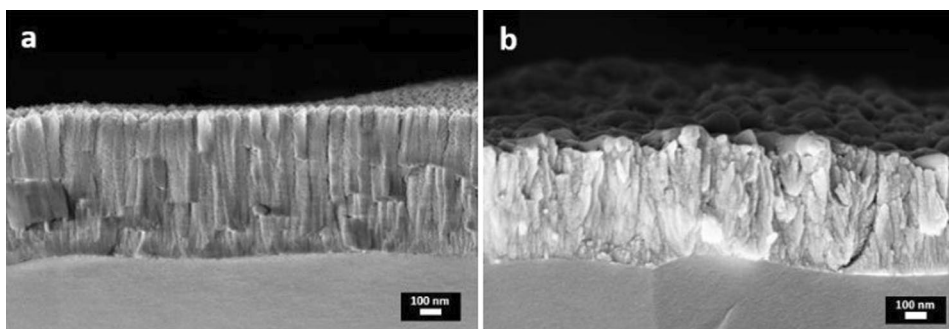


laser fluence up to 125 mJ/cm² still results in well-ordered LIPSS at $V=0.4$ mm/s (Fig. 9c1). However, at a lower scanning speed (0.2 mm/s), ablation of the thin layer of GDC takes place (Fig. 9c2). Finally, for the highest laser fluence used in this work, namely, 150 mJ/cm², GDC film ablation is observed at $V=0.4$ mm/s (Fig. 9d1) and becomes nearly complete at $V=0.2$ mm/s (Fig. 9d2). At such a speed and laser fluence, the grain boundaries of the YSZ substrate become exposed and the substrate itself becomes regularly patterned into square shaped structures, probably due to surface cracking, as observed for the highest laser fluence and number of pulses in the static irradiation case (Fig. 6j). As

indicated previously, during this ablation process we only reproduced the $LSFL_{\perp}$ before the full removal of the GDC thin film.

Figure 10 shows two SEM images of the cross section of the GDC layer. The first one is the untreated layer and the other one a layer textured by laser scanning at a fluence of 85 mJ/cm² and a velocity $V=0.4$ mm/s. First of all it is clearly visible that the GDC film in-depth microstructure changes greatly. The well-aligned columns of about 100 nm width are not present any more, and have been replaced by less regular patterns. It can also be noticed that the thickness

Fig. 10 SEM images of the transverse section of GDC: **a** untreated surface and **b** after irradiation in scanning mode at $F=85 \text{ mJ/cm}^2$ and $V=0.4 \text{ mm/s}$



of the layer has decreased by about 100 nm, which confirms the partial ablation that occurs for this condition.

In addition, RBS measurements, illustrated in Fig. 11, were performed on these two samples to confirm the thickness reduction after laser structuring. From simulation of the spectra, it can be deduced that there was a 17% decrease of the Ce and Gd atoms/cm² after laser treatment, while the proportions of YSZ and O remained unchanged. And finally, the shape of the spectra at the interface between GDC and YSZ layers indicates that the roughness of the layer increases, which is in good agreement with the SEM images of Fig. 10.

3.3 Estimation of the surface area increase by LIPSS

The surface modification due to the formation of nanostructures can be evaluated through some simple geometrical considerations. We estimated the surface enhancement

due to LIPSS fabrication using the geometrical model detailed in the Appendix. From the set of Eqs. (6* and 7*), the maximum theoretical enhancement coefficient (Σ) cannot exceed 57% in the case of regular 1D LIPSS and 78% in the case of 2D LIPSS (nanodots, nanobumps, etc.). This maximum is only achieved in the case of contiguous LIPSS, i.e., the situation for $2r \approx \Lambda$, where r is here the specific radius of the nanostructure (assumed uniform), and Λ the spatial period. However, the major cases of LIPSS configurations correspond to the case $2r/\Lambda < 1$, and as reported in Table 1, the estimation of the enhancement coefficient Σ returns values in the range of 10–40%, which is far from the theoretical values. Considering the LIPSS sizes obtained in Fig. 12 (better resolution of the cross section and tilted SEM image), we performed the same estimation of the Σ coefficient in the case of GDC and compared this value to literature values, summarized in Table 1. On the other hand, thanks to the AFM

Fig. 11 RBS spectroscopy for untreated and textured GDC/YSZ film at $F=85 \text{ mJ/cm}^2$ and $V=0.4 \text{ mm/s}$

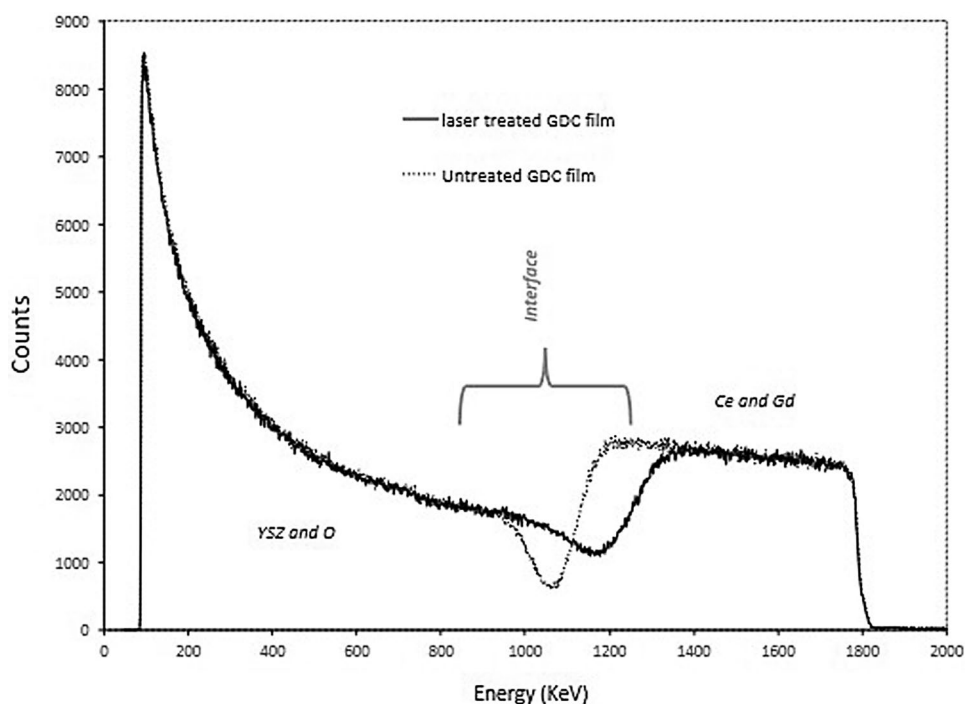


Table 1 Surface enhancement coefficient (Σ) versus LIPSS size and periods

Refs.	Laser/wavelength (nm)	Materials/nanostructures	Period		Specific size R_{eq} (nm)	Σ (%)
			λ_1 (nm)	λ_2 (nm)		
Huynh [16]	Nd:YAG (40 ps)	Cu	270	200	68	127
	266	Nano-dots 2D				
Nakhoul [1]	Ti: Sapphire (25 fs)	Ni	110	–	32	134
	800	Nano-pumps 1D				
Talbi [17]	Yb:YKW (500 fs)	TiO _{1.8}	800	–	142	120
	1030	LSFL 1D				
Gao [39]	Picosecond laser (8 ps)	Si	528	–	104	122
	532	LSFL 1D				
Bonse [40]	Ti:sapphire (150 fs)	Ti	590	–	171	133
	800	LSFL 1D				
Talbi [41]	Ti:sapphire (100 fs)	TiO _x	400	200	50	110
	266	Nano-spikes 2D				
Ehrhardt [42]	Fibre laser (25 ns)	SiO ₂	500	–	163	137
	1064	LSFL 1D				
Parellada-Monreal [43]	Ti: Sapphire (130 fs)	ZnO	145	–	50	140
	800	HSFL 1D				
Dostavalov [31]	PHAROS 6 W laser (232 fs)	Cr	696	–	155	125
	1064	LSFL _{//} , LSFL _⊥				
This work	Nd:YAG (40 ps) 355	GDC	240	–	76	136
		LSFL _{//}				
		LSFL _⊥	280	–	70	125
		Nanosquared LIPSS	240	300	100	141

mathematical toolbox, it was possible to estimate directly the GDC surface morphology changes before and after the beam irradiation in the conditions $F = 85 \text{ mJ/cm}^2$ and $V = 0.4 \text{ mm/s}$. In this case, the difference between the irradiated film surface and the ‘as deposited’ one was estimated to be close to 40% (42% in the case of a $5 \times 5 \mu\text{m}^2$

AFM scanned zone, and 39% for the case $2 \times 2 \mu\text{m}^2$). Both values are relatively high compared to the literature cases, and in good agreement with the calculated Σ coefficient, namely, for the case of the nanosquared LIPSS (superposition of parallel and perpendicular LIPSS).

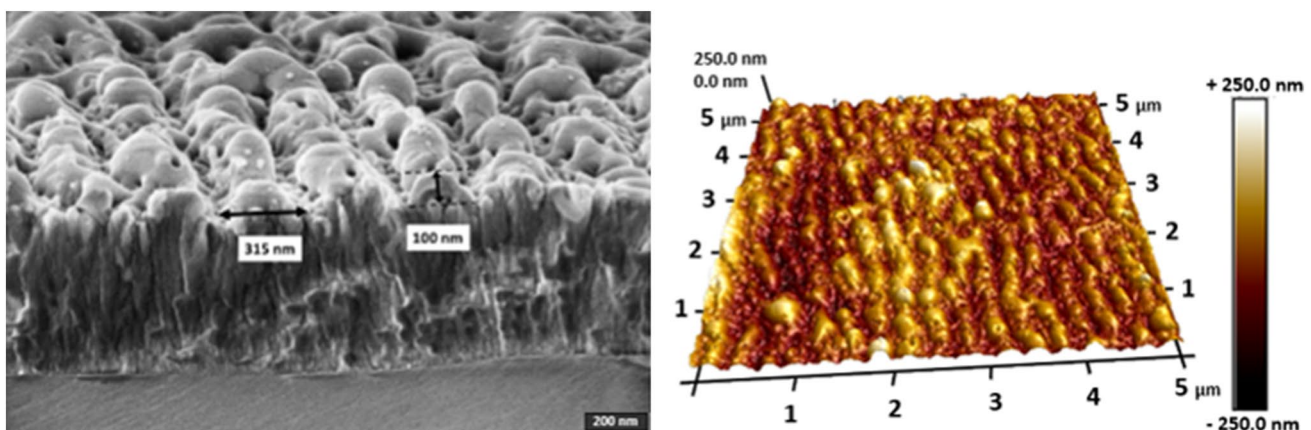


Fig. 12 SEM and 3D AFM images of the cross section of ‘nanosquared’ GDC/YSZ film for $F = 85 \text{ mJ/cm}^2$, $V = 0.4 \text{ mm/s}$

3.4 Conclusions

We demonstrated the feasibility of nanostructuring with quasi-periodic LIPSS GDC sputtered films deposited onto a screen-printed YSZ substrate using a UV picosecond laser beam with a low repetition rate. Static and scanning irradiation modes were investigated according to the fluence and number of pulses. In the static mode, two unexpected LSFL orientations were formed within the same irradiated area for F varying from 85 up to 125 mJ/cm² but only for a low number of accumulated pulses ($N < 20$). The formation of parallel LSFL is supported by the thermochemical oxidation origin and the transition to the MIEC state that occurs in the center of the irradiated zone for higher accumulated energy doses. With higher numbers of pulses, the GDC film is progressively ablated, resulting in the step-by-step removal of the film followed by the square-like patterning of the YSZ substrate. In the dynamic mode and for equivalent conditions $F = 85$ mJ/cm² and $N_{\text{eff}} = 25$, LSLF were formed on a large area (4X4 mm²) with a perpendicular orientation, whereas a more complex patterning was achieved at $F = 125$ mJ/cm², and $N_{\text{eff}} = 10$ attributed to the overlap and the superposition of parallel and perpendicular LSFL. The scanning limits leading to the progressive ablation of the GDC film were also investigated until the full removal of the film and the starting point of YSZ substrate patterning. Lastly, the enhancement of the exchange surface area estimated by a simple geometrical model and direct AFM measurements for the condition $F = 85$ mJ/cm² and $V = 0.4$ mm/s is estimated to be close to 33% for LSFL// and to 40% for the nanosquared LIPSS.

Supplementary Information The online version contains supplementary material available at <https://doi.org/10.1007/s00339-022-05866-6>.

Acknowledgements The authors would like to thank *Julien Vulliet* from the CEA Le Ripault for providing the screen-printed YSZ substrates, and the 'Région Centre-Val-de-Loire' for funding via the 'ARD Lavoisier' program.

Declarations

Conflict of interest The authors declare no conflict of interest.

References

1. A. Nakhoul et al., Self-organization regimes induced by ultrafast laser on surfaces in the tens of nanometer scales. *Nanomaterials* (2021). <https://doi.org/10.3390/nano11041020>
2. L.P. Rivera, D. Munoz-Martin, A. Chávez-Chávez, M. Morales, G. Gómez-Rosas, C. Molpeceres, Subwavelength LIPSS formation on SS304 by picosecond laser irradiation under water confinement. *Mater. Sci. Eng. B* **273**, 115393 (2021). <https://doi.org/10.1016/j.mseb.2021.115393>
3. H. Bonse, D.S. Sturm, W. Kautek, Chemical, morphological and accumulation phenomena in ultrashort-pulse laser ablation of TiN in air. *Appl. Phys. Mater. Sci. Process.* (2000). <https://doi.org/10.1007/s003390000585>
4. A. Borowiec, H.K. Haugen, Subwavelength ripple formation on the surfaces of compound semiconductors irradiated with femtosecond laser pulses. *Appl. Phys. Lett.* (2003). <https://doi.org/10.1063/1.1586457>
5. A. De Zanet, V. Casalegno, M. Salvo, Laser surface texturing of ceramics and ceramic composite materials—a review. *Ceram. Int.* (2021). <https://doi.org/10.1016/j.ceramint.2020.11.146>
6. F. Costache, M. Henyk, J. Reif, Modification of dielectric surfaces with ultra-short laser pulses. *Appl. Surf. Sci.* (2002). [https://doi.org/10.1016/S0169-4332\(01\)00675-4](https://doi.org/10.1016/S0169-4332(01)00675-4)
7. Q. Li et al., Femtosecond laser-induced periodic surface structures on lithium niobate crystal benefiting from sample heating. *Photonics Res.* (2018). <https://doi.org/10.1364/PRJ.6.000789>
8. E. Stratakis et al., Laser engineering of biomimetic surfaces. *Mater. Sci. Eng. R Rep.* **141**, 100562 (2020). <https://doi.org/10.1016/j.mser.2020.100562>
9. J. Bonse, S. Hohm, S.V. Kirner, A. Rosenfeld, J. Kruger, Laser-induced periodic surface structures—a scientific evergreen. *IEEE J. Sel. Top. Quantum Electron.* (2017). <https://doi.org/10.1109/JSTQE.2016.2614183>
10. M. Ahn et al., Low damage electrical modification of 4H-SiC via ultrafast laser irradiation. *J. Appl. Phys.* **123**(14), 145106 (2018). <https://doi.org/10.1063/1.5020445>
11. A.Y. Vorobyev, C. Guo, Direct femtosecond laser surface nano/microstructuring and its applications. *Laser Photon. Rev.* (2013). <https://doi.org/10.1002/lpor.201200017>
12. J. Reif, O. Varlamova, S. Uhlig, S. Varlamov, M. Bestehorn, On the physics of self-organized nanostructure formation upon femtosecond laser ablation. *Appl. Phys. A* (2014). <https://doi.org/10.1007/s00339-014-8339-x>
13. E.L. Gurevich, S.V. Gurevich, Laser induced periodic surface structures induced by surface plasmons coupled via roughness. *Appl. Surf. Sci.* **302**, 118–123 (2014). <https://doi.org/10.1016/j.apsusc.2013.10.141>
14. P. Liu, W. Wang, A. Pan, Y. Xiang, D. Wang, Periodic surface structures on the surface of indium tin oxide film obtained using picosecond laser. *Opt. Laser Technol.* **106**, 259–264 (2018). <https://doi.org/10.1016/j.optlastec.2018.04.019>
15. C. Deng et al., Photocatalytic performance of TiO₂ thin film decorated with Cu₂O nanoparticles by laser ablation. *Opt. Mater.* **94**, 130–137 (2019). <https://doi.org/10.1016/j.optmat.2019.05.030>
16. T.T.D. Huynh, A. Petit, N. Semmar, Picosecond laser induced periodic surface structure on copper thin films. *Appl. Surf. Sci.* **302**, 109–113 (2014). <https://doi.org/10.1016/j.apsusc.2013.10.172>
17. A. Talbi et al., Femtosecond laser irradiation of titanium oxide thin films: accumulation effect under IR beam. *Appl. Phys. A* (2020). <https://doi.org/10.1007/s00339-020-03568-5>
18. O. Varlamova, F. Costache, M. Ratzke, J. Reif, Control parameters in pattern formation upon femtosecond laser ablation. *Appl. Surf. Sci.* **253**(19), 7932–7936 (2007). <https://doi.org/10.1016/j.apsusc.2007.02.067>
19. J. Bonse, A. Rosenfeld, J. Krüger, On the role of surface plasmon polaritons in the formation of laser-induced periodic surface structures upon irradiation of silicon by femtosecond-laser pulses. *J. Appl. Phys.* (2009). <https://doi.org/10.1063/1.3261734>
20. J. Bonse, J. Krüger, Pulse number dependence of laser-induced periodic surface structures for femtosecond laser irradiation of silicon. *J. Appl. Phys.* (2010). <https://doi.org/10.1063/1.3456501>
21. S.K. Das, H. Messaoudi, A. Debroy, E. McGlynn, R. Grunwald, Multiphoton excitation of surface plasmon-polaritons and scaling

- of nanoripple formation in large bandgap materials. *Opt. Mater. Express* (2013). <https://doi.org/10.1364/OME.3.001705>
22. A. Nechache, S. Hody, Alternative and innovative solid oxide electrolysis cell materials: a short review. *Renew. Sustain. Energy Rev.* **149**, 111322 (2021). <https://doi.org/10.1016/j.rser.2021.111322>
 23. B. Butz, Yttria-doped zirconia as solid electrolyte for fuel-cell applications. *Laboratorium für Elektronenmikroskopie (LEM)*, 2009.
 24. B. Steele, Appraisal of $Ce_{1-y}Gd_yO_{2-y/2}$ electrolytes for IT-SOFC operation at 500°C. *Solid State Ion.* (2000). [https://doi.org/10.1016/S0167-2738\(99\)00319-7](https://doi.org/10.1016/S0167-2738(99)00319-7)
 25. M. Mickan, P. Coddet, J. Vulliet, A. Caillard, T. Sauvage, A.-L. Thomann, Optimized magnetron sputtering process for the deposition of gadolinia doped ceria layers with controlled structural properties. *Surf. Coat. Technol.* **398**, 126095 (2020). <https://doi.org/10.1016/j.surfcoat.2020.126095>
 26. J. Bonse, Quo Vadis LIPSS?—recent and future trends on laser-induced periodic surface structures. *Nanomaterials* **10**(10), 1950 (2020). <https://doi.org/10.3390/nano10101950>
 27. J. Reif, F. Costache, M. Henyk, S.V. Pandelov, Ripples revisited: non-classical morphology at the bottom of femtosecond laser ablation craters in transparent dielectrics. *Appl. Surf. Sci.* **197–198**, 891–895 (2002). [https://doi.org/10.1016/S0169-4332\(02\)00450-6](https://doi.org/10.1016/S0169-4332(02)00450-6)
 28. M. Mezera, J. Bonse, G.R.B.E. Römer, Influence of bulk temperature on laser-induced periodic surface structures on polycarbonate. *Polymers* **11**(12), 1947 (2019). <https://doi.org/10.3390/polym11121947>
 29. E. Rebollar, M. Castillejo, T.A. Ezquerro, Laser induced periodic surface structures on polymer films: from fundamentals to applications. *Eur. Polym. J.* **73**, 162–174 (2015). <https://doi.org/10.1016/j.eurpolymj.2015.10.012>
 30. O. Shavdina, H. Rabat, M. Vayer, A. Petit, C. Sinturel, N. Semmar, Polystyrene thin films nanostructuring by UV femtosecond laser beam: from one spot to large surface. *Nanomaterials* (2021). <https://doi.org/10.3390/nano11051060>
 31. A.V. Dostovalov et al., LIPSS on thin metallic films: new insights from multiplicity of laser-excited electromagnetic modes and efficiency of metal oxidation. *Appl. Surf. Sci.* **491**, 650–658 (2019). <https://doi.org/10.1016/j.apsusc.2019.05.171>
 32. J. Bonse, S. Gräfm, Maxwell meets marangoni—a review of theories on laser-induced periodic surface structures. *Laser Photon. Rev.* **14**, 2000215 (2020). <https://doi.org/10.1002/lpor.202000215>
 33. J.E. Sipe, J.F. Young, J.S. Preston, H.M. van Driel, Laser-induced periodic surface structure. I. Theory. *Phys. Rev. B* (1983). <https://doi.org/10.1103/PhysRevB.27.1141>
 34. A.V. Dostovalov, V.P. Korolkov, K.A. Okotrub, K.A. Bronnikov, S.A. Babin, Oxide composition and period variation of thermochemical LIPSS on chromium films with different thickness. *Opt. Express* **26**(6), 7712 (2018). <https://doi.org/10.1364/OE.26.007712>
 35. B. Öktem et al., Nonlinear laser lithography for indefinitely large-area nanostructuring with femtosecond pulses. *Nat. Photon.* **7**(11), 897–901 (2013). <https://doi.org/10.1038/nphoton.2013.272>
 36. S.R. Bishop, K.L. Duncan, E.D. Wachsmann, Thermo-chemical expansion in strontium-doped lanthanum cobalt iron oxide: thermo-chemical expansion in LSCF. *J. Am. Ceram. Soc.* **93**(12), 4115–4121 (2010). <https://doi.org/10.1111/j.1551-2916.2010.03991.x>
 37. Y. Kuru, M. Usman, G. Cristiani, H.-U. Habermeier, Microstructural changes in epitaxial $YBa_2Cu_3O_{7-\delta}$ thin films due to creation of O vacancies. *J. Cryst. Growth* **312**(20), 2904–2908 (2010). <https://doi.org/10.1016/j.jcrysgro.2010.06.030>
 38. S.R. Bishop, H.L. Tuller, Y. Kuru, B. Yildiz, Chemical expansion of nonstoichiometric $Pr_{0.1}Ce_{0.9}O_{2-\delta}$: correlation with defect equilibrium model. *J. Eur. Ceram. Soc.* **31**(13), 2351–2356 (2011). <https://doi.org/10.1016/j.jeurceramsoc.2011.05.034>
 39. Y.-F. Gao et al., Picosecond laser-induced periodic surface structures (LIPSS) on crystalline silicon. *Surf. Interfaces* **19**, 100538 (2020). <https://doi.org/10.1016/j.surfin.2020.100538>
 40. J. Bonse, J. Krüger, S. Höhm, A. Rosenfeld, Femtosecond laser-induced periodic surface structures. *J. Laser Appl.* (2012). <https://doi.org/10.2351/1.4712658>
 41. A. Talbi, C.T. Tameko, A. Stolz, E. Millon, C. Boulmer-Leborgne, N. Semmar, Nanostructuring of titanium oxide thin film by UV femtosecond laser beam: from one spot to large surfaces. *Appl. Surf. Sci.* **418**, 425–429 (2017). <https://doi.org/10.1016/j.apsusc.2017.02.033>
 42. M. Ehrhardt, B. Han, F. Frost, P. Lorenz, K. Zimmer, Generation of laser-induced periodic surface structures (LIPSS) in fused silica by single NIR nanosecond laser pulse irradiation in confinement. *Appl. Surf. Sci.* **470**, 56–62 (2019). <https://doi.org/10.1016/j.apsusc.2018.11.119>
 43. L. Parellada-Monreal, I. Castro-Hurtado, M. Martínez-Calderón, L. Presmanes, G.G. Mandayo, Laser-induced periodic surface structures on ZnO thin film for high response NO_2 detection. *Appl. Surf. Sci.* **476**, 569–575 (2019). <https://doi.org/10.1016/j.apsusc.2019.01.115>

Publisher's Note Springer Nature remains neutral with regard to jurisdictional claims in published maps and institutional affiliations.

Springer Nature or its licensor holds exclusive rights to this article under a publishing agreement with the author(s) or other rightsholder(s); author self-archiving of the accepted manuscript version of this article is solely governed by the terms of such publishing agreement and applicable law.

Authors and Affiliations

Wael Karim¹ · Agnès Petit¹ · Hervé Rabat¹ · Malek Tabbal² · Anne-Lise Thomann¹ · Nadjib Semmar¹ 

✉ Nadjib Semmar
Nadjib.semmar@univ-orleans.fr

² Department of Physics, American University of Beirut, Beirut 1107 2020, Lebanon

¹ GREMI-UMR 7344-CNRS-University of Orleans, 14 Rue d'Issoudun, BP 6744, 45067 Orléans Cedex, France